

1
2 **Evidence of magma activation beneath the Lunayyir basaltic field (Saudi**
3 **Arabia) from attenuation tomography**
4

5 Ivan Koulakov^{1,2} (ivan.science@gmail.com, corresponding author),

6 Sami El Khrepy^{3,4} (k_sami11@yahoo.com),

7 Nassir Al-Arifi³ (nalarifi@ksu.edu.sa),

8 Ilya Sychev¹ (ilya.sychev@gmail.com)

9 Pavel Kuznetsov¹ (kuznecov.p.u@gmail.com)

- 10
- 11 1. Trofimuk Institute of Petroleum Geology and Geophysics SB RAS, Prospekt Koptyuga, 3,
12 630090, Novosibirsk, Russian Federation, ,
 - 13 2. Novosibirsk State University, Novosibirsk, Russia, Pirogova 2, 630090, Novosibirsk,
14 Russia
 - 15 3. King Saud University, Riyadh, Saudi Arabia, P.O. Box 2455, Riyadh 11451, Saudi
16 Arabia.
 - 17 4. National Research Institute of Astronomy and Geophysics, NRIAG, 11421, Helwan,
18 Egypt.
- 19
20
21

22 submitted to Solid Earth

23 Novosibirsk, Riyadh,

24 July, 2014

25

26 **Evidence of magma activation beneath the Lunayyir basaltic field (Saudi**
27 **Arabia) from attenuation tomography**

28 Ivan Koulakov, Sami El Khrepy, Nassir Al-Arifi, Ilya Sychev, and Pavel Kuznetsov

29

30 **Abstract**

31 We present a seismic attenuation model for the crust beneath the Cenozoic basaltic field of
32 Lunayyir (western Saudi Arabia), where a strong seismic swarm occurred in 2009. The
33 tomography inversion uses the envelope shape of the S-wave seismograms from over 300 strong
34 events ($M > 3.5$). The resulting attenuation structures appear to be consistent with the distribution
35 of seismic velocities. The obtained 3D attenuation model distinguishes the low-attenuation zones
36 down to 5 km depth corresponding to the rigid basaltic cover. At greater depths, we detect a
37 high-attenuation anomaly coinciding with the main seismicity cluster. We propose that this zone
38 corresponds to the upper part of the conduit area ascending from deeper magma sources.
39 According to the distributions of local events, fluids and melts from this conduit appear to reach
40 a depth of ~ 2 km, but were not able to reach the surface and cause the eruption in 2009.

41

42 **Key words:** Seismic Attenuation, Harrat Lunayyir, Seismicity Swarm, Saudi Arabia, Magma
43 Conduit

44

45 **1. Introduction.**

46 The western part of the Arabian Peninsula is characterized by a wide distribution of
47 Cenozoic basaltic fields (harrats). Some of these fields are still active and present a real eruption
48 potential. During the human history time there were several records of eruptions occurred within
49 the harrats of Saudi Arabia and Yemen (e.g., *Camp et al., 1987*). The harrats are located close to
50 the western coast of the Arabian Peninsula, and their appearance is thought to be linked to the
51 rifting of the Red Sea (e.g., *Cochran, Martinez, 1988*). However, the role that the opening of the

52 Red Sea played in the origination of Lunayyir and other harrats appears to be rather complex.
53 Unlike the southern Red Sea segment, which has a clear ocean-type spreading, the extension of
54 the northern segment appears to result from the stretching of the continental crust at a rate of ~10
55 mm/year (*Cochran, Karner, 2007*). According to regional tomography studies (e.g., *Chang et al.,*
56 *2011*), no low-velocity anomalies, which could be associated with hot areas, have been observed
57 beneath the Red Sea. Instead, negative seismic anomalies align beneath the western part of the
58 Arabian plate exactly where the volcanic fields are located. These observations may give
59 arguments for the passive character of rifting in the Northern Red Sea. However the lithosphere
60 extension may cause the asthenosphere upwelling beneath the coastal areas that is responsible for
61 the volcanic activity.

62 Lunayyir is one of the youngest harrats in Saudi Arabia (less than 1 Ma, *Pallister et al.*
63 *2010*), and it is small relative to other Cenozoic basaltic fields in the Arabian Peninsula. In
64 Lunayyir, recent basalts cover an area that is over 3500 km² in size (*Figure 1b*). The last eruption
65 in this area occurred approximately 1000 years ago (*Camp et al., 1987*); however, elevated
66 groundwater temperatures and the existence of fumaroles indicate that strong thermal activities
67 still occur in this zone (e.g., *Al-Dayel, 1988*). This volcanic field is considered a probable
68 candidate for the next eruption. Before 2009, weak to moderate seismicity mostly associated
69 with tectonic crustal displacements in the Red Sea and Gulf of Aqaba was observed in this area
70 (e.g., *El-Isa and Al-Shanti, 1989; Al-Amri, 1995*). In April-July 2009, a strong swarm of over
71 30,000 earthquakes reaching a magnitude of 5.4 occurred in the Lunayyir area. Most of these
72 events were confined to have been oriented along a NNW-SSE line that was approximately 20
73 km long in the northern part of the Harrat (*Figure 1b*). This seismicity included both high- and
74 low-frequency events (*Pallister et al., 2010*) that might indicate the potential volcanic nature of
75 this swarm. This hypothesis was supported by models based on InSAR and geodetic data
76 developed by *Baer and Hamiel, (2010)* who proposed a vertical dyke intrusion.

77 Questions relating to the origin of this swarm and the possible continuation of these
78 processes lead to vital discussions in the scientific community. Studying the deep structure
79 beneath the Lunayyir area can greatly help with understanding these problems. The spatial and
80 temporal distributions of the seismicity and earthquake mechanisms were carefully studied by
81 *Zobin et al., (2013)*. They compared the main seismic activity features to several volcanoes
82 around the world and concluded that a further volcanic awaking was not plausible for the
83 Lunayyir area. However, most other authors studying different aspects of this problem have
84 suggested future volcanic intrusions were likely. In particular, the recent seismic tomography
85 study by *Hansen et al. (2013)* discovered a high P-velocity body that was interpreted as an area
86 with repeated magmatic intrusions. This result was obtained based on the accurate, double-
87 difference location of over 5000 seismic events and the tomographic inversion of P-wave arrival
88 times from local earthquakes. At the same time, the local earthquake tomography suffered a
89 trade-off between the velocity structure and the source parameters, which should be
90 simultaneously determined during the inversion. With highly concentrated source locations, such
91 as those found beneath the Lunayyir area, the velocity around the seismicity cluster might appear
92 to be poorly resolved because of trade-offs among the seismic velocity, origin time and event
93 depth. When only P-data are used, the situation worsens. Therefore, we propose that the results
94 of *Hansen et al. (2013)* should be carefully tested in independent studies using different methods.

95 In this study, we present attenuation tomography results for the same area studied by
96 *Hansen et al. (2013)*. The advantage of attenuation tomography over the velocity local
97 earthquake tomography is that it addresses the linearized inverse problem, which affects neither
98 the source localization nor the ray paths and requires only one inversion iteration. For slightly
99 mislocated sources, the **location of the retrieved attenuation patterns** can be slightly biased;
100 however, this effect generally appears minor during interpretation. In addition, the attenuation
101 parameters are more sensitive to the fracture distribution and liquid phase content (fluids and
102 melts), which seem to be important for determining the origin of the Lunayyir activation.

103 Seismic tomography is a powerful tool for studying magmatic sources beneath volcanic
104 areas (see, for example, overviews in *Lees, 2007* and *Koulakov, 2013*, which present several
105 successful examples of tomography studies of volcanoes). Attenuation tomography has been
106 successfully used in many studies of crustal and mantle structures. Regional attenuation
107 structures in the mantle beneath the Arabian plate surrounding the studied region were
108 investigated together with Pn and Sn velocities by *Al-Damegh et al., (2004)*. They found a
109 presence of a large mantle anomaly beneath western Arabia which is interpreted as zone of
110 thinner lithosphere and hot asthenosphere. The attenuation tomography was used for studying
111 crustal structures beneath volcanoes in different regions using active source data, such as in case
112 of Medicine Lake in California *Evans and Zucca (1988)*, and passive source data, including
113 Loma Prieta (*Lees and Lindley, 1994*), Etna (*Martínez-Arévalo et al., 2005*), Central Andes
114 (*Shurr et al., 2003, Koulakov et al., 2006*), and Kilauea (*Hansen et al., 2004*). In case of dormant
115 volcanoes, these studies generally identified lower attenuation zones beneath volcanoes, whereas
116 in cases of active volcanoes, they found contrasted patterns of higher attenuation. Most of these
117 studies used a technique based on retrieving t^* by analyzing waveforms around P-wave arrivals.
118 The t^* values of the S-waves at different frequencies were used in some studies, such as the
119 tomographic inversion of the North-Anatolian fault (*Koulakov et al., 2010*). A similar approach
120 was used in the present study; however, instead of using t^* , we estimated the attenuation
121 parameter by analyzing the envelope shape of the S-wave signal, as proposed in the classic work
122 by *Aki and Chouet (1975)*. In this study, we provide the seismic attenuation distribution beneath
123 the Lunayyir area, which helps us understand the origin of recent seismic activities.

124

125 **2. Data and Algorithms**

126 After the beginning of the seismic crisis in April 2009, a seismic network was installed in
127 the Lunayyir area by the King Abdulaziz City of Science and Technology (KACST), King Saud
128 University (KSU), and the Saudi Geological Survey (SGS). Data for over 5700 events using

129 autopicked P-arrival times were used by *Hansen et al. (2013)*. In this study, we manually re-
130 analyzed the same waveform data. We selected 1879 strong events with the magnitudes above
131 3.2 and identified 8904 P- and 10579 S-phases for most of these events at the available stations,
132 which enabled the robust locating of the sources. It is interesting there were slightly more S-
133 phases than P-phases, which can be explained by the clearer and stronger S-wave signal. These
134 data were used to run a simultaneous tomographic inversion for P- and S-velocities and source
135 locations based on the iterative LOTOS algorithms (*Koulakov, 2009*). The results of the velocity
136 inversion are described in details in (*Koulakov et al., 2014*). The resulting velocity model, which
137 is presented in [Figure 2](#), is used in this study as the background model for the attenuation
138 tomography.

139 After performing the source locations, we analyzed the seismograms of every source-
140 receiver pair to estimate the attenuation parameters of each ray. We used the basic attenuation
141 estimation principles proposed in the classic work of *Aki and Chouet (1975)*. The physical
142 background of the method is schematically illustrated in [Figure 3](#). We are studying the intrinsic
143 attenuation, which is responsible for conversion of a part of the seismic energy into the heat and
144 leads to the decrease of the amplitude of seismic signal on the seismogram. However direct
145 deriving the attenuation values from measurement of the amplitude of seismic signal is an
146 ambiguous task, because the amplitude may be also affected by a variety of different factors,
147 such as source characteristics, geometrical spreading, focusing/defocusing, scattering, reflections
148 etc. Studying the properties of seismic signal following the main wave arrival (seismic coda)
149 provides more information on the medium intrinsic attenuation. For example, striking a piece of
150 metal with low attenuation yields a sound that is affected by the existence of numerous scatterers
151 and reflectors that can be heard for a rather long time (long flat coda). Alternatively, sound from
152 a highly attenuated wooden balk would be much shorter (short coda). When studying the earth
153 structures, it is presumed that the medium contains a large amount of scatters which are more or
154 less uniformly distributed throughout the space (hatches in [Figure 3](#)). In this case, besides the

155 direct wave there are infinite number of secondary scattering waves which compose the coda.
 156 The properties of the coda depend on the properties of the medium in which the main and
 157 scattered waves propagate. In case of highly attenuated medium (e.g., corresponding to station B
 158 in [Figure 3](#)) more energy of the seismic waves will be converted into the heat and this causes
 159 stronger decay of the envelop amplitude compared to the direct wave. For the low-attenuation
 160 medium (case of station A) the coda decrement is longer. [Aki and Chouet \(1975\)](#) approximated
 161 the envelope for seismic code after the arrival of the main wave using an exponential dependence:

$$162 \quad A(f, t) = t^{-\beta} A_0 \exp\left(\frac{-\pi ft}{Q(f)}\right) \quad (1)$$

163 where t is travel time, A_0 is the signal amplitude in the source area, f is its frequency, and
 164 $Q(f)$ is a quality factor (inverse of the attenuation). [Figure 4A](#) shows a real seismogram
 165 corresponding to the horizontal component filtered at 3 Hz. The envelope of the waveform is
 166 shown in [Figure 4B](#). Applying a logarithmic transformation and then smoothing (central moving
 167 average in a 2-s interval) provides the curve shown in [Figure 4C](#), which can be approximated
 168 using a straight line directly associated to the attenuation:

$$169 \quad \ln(A(f, t)) + \beta \ln(t) = \ln(A_0) - \frac{-\pi ft}{Q(f)} \quad (2)$$

170 The effect of geometrical spreading can be easily estimated using existing seismic ray
 171 parameters in the existing velocity model. Thus, the slope of the fit line shown in [Figure 4C](#) is
 172 proportional to the attenuation value, $1/Q$. For example, a gentle slope (long code) indicates a
 173 high-quality factor and low attenuation. To avoid small numbers in the output from the
 174 tomography inversion, we use the inverse of the attenuation multiplied by 1000. Because of the
 175 uncertainty in A_0 , we cannot obtain an absolute value for the quality factor. Therefore, we use
 176 the average estimated values as a reference for the quality factor. We computed the relative
 177 positive and negative deviations in the quality factor for the inversion with respect to the
 178 reference value.

179 In the analysis of seismograms, we consider a 10-s lapse window starting at 1 s after the
180 arrival of the S-phase. This is different of a common way for computing the slope of the Q-coda
181 which is usually based on the two travel times of the S-wave as a starting point (e.g., *Aki, 1980,*
182 *Rautian and Khalturin, 1979*). We could not use the traditional definition of coda because for
183 most events the signal was not very strong. After the moment of two S-travel times, the low
184 signal/noise ratio made the determinations of the coda characteristics very unstable. The delay of
185 1 s seems to us optimal to start the lapse window as corresponding to the maximum amplitude of
186 the direct waves. Just after the first arrival, the shape of the seismogram is dependent on the
187 source properties and usually not reaches the maximum immediately. In our experience, the best
188 exponential approximation for the coda decrement can be obtained for the window starting close
189 to the moment of maximum of the direct wave. Comparing the amplitudes of direct and
190 secondary waves seems to be more stable than the analysis of only secondary waves, which are
191 strongly affected by many different factors (such as distribution of scatters). We made several
192 attempts of using other criteria for defining the start of the lapse times (such as two S-times) but
193 obtained unstable solutions which were inconsistent for different frequencies. In this sense, here
194 we implement not commonly used estimate for slope of the Q-coda, but the measurement of how
195 large is the S-wave packet compared to the coda waves (see for a wide discussion about this
196 topic in *Sato and Fehler, (1998)* and *Gusev and Abubakirov, (1999)*). In other word, this Q-coda
197 parameter matches more to the measure of the S-wave envelope broadening than directly to the
198 estimation of the attenuation parameter along the ray path.

199 The data were independently processed across narrow-band-filtered seismograms with six
200 different frequencies: 0.75, 1.50, 3, 6, 12 and 24 Hz. The processing results were carefully
201 visually inspected for each ray. As a result, many data were rejected for not providing a clear
202 linear approximation; only 4326 values had a sufficiently high quality for the inversion.

203 The attenuation tomographic inversion algorithm was generally identical to the first
204 iteration step of the LOTOS code (*Koulakov, 2009*), which was initially designed for travel time

205 passive source tomography. In our case, the source locations were obtained at a previous step of
206 velocity tomography and remained unchanged when computing the attenuation. The rays were
207 constructed using a bending ray tracer in the previously constructed 3D S-velocity model based
208 on the travel time tomography (same as shown in Figure 2). Note that the velocity model may
209 affect the locations of sources. However, we performed the attenuation reconstructions using
210 different velocity models and found that changes in the velocity model have minor effect upon
211 the computed attenuation models. An example of the attenuation model derived based on the 1D
212 velocity distribution is shown in Figure 5. It can be seen that the locations of sources is slightly
213 different of those in the main model (Figure 6), which is based on the best 3D velocity model,
214 but the configuration of the main attenuation patterns looks similar in these two cases. In this
215 sense, the attenuation results appear to be not strongly dependent on the reference velocity
216 models.

217 The ray coverage was used to construct a parameterization grid with nodes distributed
218 according to the data density. The horizontal grid spacing was 2 km; in the vertical direction, the
219 distances between nodes depended on the ray coverage and were not smaller than 0.5 km.
220 Between the nodes, the velocity was linearly interpolated. To reduce the grid dependency of the
221 results, we performed the inversion for four grids with different basic orientations and then
222 average the computed models and then compute the average model based on the uniform mesh.
223 The first derivative matrix, A_{ij} , represents the numerically computed effect of unit variation in
224 the i -th node upon the cumulative attenuation of the j -th ray for rays traced in the 3D model.
225 This matrix was inverted using the LSQR algorithm (*Paige and Saunders, 1982*). This algorithm
226 uses only non-zero matrix elements and performs the iterative line-by-line proceeding of the
227 matrix. This allows solving large linear equation systems using modest computing resources.
228 The solution stability was controlled using an additional matrix block to damp the difference
229 between neighboring nodes, which allows for the smoothing of the model.

230 The model resolution was checked using the synthetic tests presented in [Figure 7](#). In the
231 map view, the synthetic model has four positive and negative anomalies 6×6 km in size that
232 change signs at a depth of 6 km. The inversion provides a fair reconstruction of the general
233 locations of these anomalies; however, their outside contours look deformed, and there is some
234 leakage of anomalies to the initially homogeneous areas. Such distortions should be accounted
235 for when interpreting the observed data inversion results. Notably, the attenuation tomography
236 provides a much more stable reconstruction than expected when using travel time data from
237 passive sources.

238

239 **3. Discussion of the results.**

240 A comparison of the results obtained using three different frequencies is presented in
241 [Figure 8](#). It can be seen that for the shallower section the results at different frequencies appear
242 to be fairly similar: in the central part we observe low-attenuation anomaly surrounded by
243 prominent high attenuation patterns. For the deeper section, the difference appears to be more
244 important. It might be partly due to different sensitivity of attenuation parameters at different
245 frequencies. It should also be noted, that based on the visual analysis of data, the quality of
246 attenuation retrieval at 3Hz was much higher than in the cases of other frequencies. That is why,
247 the model corresponding to 3 Hz frequency was selected as the main result of this study.

248 [Figure 6](#) shows the resulting attenuation distributions in the vertical and horizontal
249 sections based on data filtered at 3 Hz. For reference, the basaltic flow limits are shown in the
250 horizontal sections. The most reliable results were obtained in the northern part of the study area;
251 the anomalies in the southernmost parts should be interpreted prudently. [This result can be](#)
252 [compared with seismic velocities obtained earlier. It is hard to make the comparison with the P-](#)
253 [velocity model computed by Hansen et al., \(2013\) because they only presented absolute](#)
254 [velocities in parallel vertical S-N sections located close to each other. In section 2, which](#)
255 [roughly correspond to these profiles, our model demonstrates a transition from low attenuation to](#)

256 the north to high attenuation to the south. This seems to be consistent with high- and low-
257 velocity anomalies in the Hansen et al. (2013) model. Much clearer correspondence is observed
258 with the velocity model by Koulakov et al., (2014) which is presented in Figure 2. Especially
259 good fit with the attenuation is achieved for the V_p/V_s ratio which is most sensitive to the
260 distributions of fluids and melts. The areas of higher V_p/V_s ratio generally match to the areas of
261 high attenuation and vice versa. The consistency of these models confirms the robustness of the
262 derived seismic models.

263 The attenuation patterns appear to match with the some geological units. For the 2-km-
264 deep shallow section, the northern boundary of the basaltic field corresponds to the transition
265 between high and low attenuations. Areas with low attenuation (high quality factors) correspond
266 to rigid igneous rocks in the harrat, whereas “red” high-attenuation areas contain softer
267 sediments. Although the high attenuation areas to the east and south of the study area are less
268 robustly resolved, they also tend to be located near the boundary of or outside the basaltic field.

269 In the 10-km-deep section, the basaltic field boundary transitions remain unchanged from
270 the shallow section. However, the brightest feature at this depth was a prominent, high-
271 attenuation anomaly that coincides with the seismicity distribution. Note that the elongated “tale”
272 of this anomaly expanded to the SE direction possibly caused by radial smearing which may
273 disturb the model, as seen in the synthetic tests (Figure 7). We see that the upper limit of this
274 high-attenuation anomaly is approximately at 6 km depth for both vertical sections. The
275 synthetic tests using the checkerboard models have a sign transition at the same depth, which
276 indicates that these depth estimates are reliable. In the WE section, the seismicity in the narrow
277 cluster is mostly located within this anomaly; however, a portion of it expands into the upper
278 low-attenuation area. In the NS section, the earthquake distribution is more scattered; however,
279 the lower limit of the seismicity cluster clearly dips southward. In the northern part, most of
280 events occur above 7 km in depth, while the events observed in the southern part occur at depths

281 of 20 km and below. This section shows the general fit for the lower limit of the seismicity
282 clusters with high attenuation.

283 We propose that the local high-attenuation anomaly beneath the central part of the study
284 area may represent a conduit zone that can bring fluids and melts from deeper sources. The
285 seismicity during the Lunayyir crisis in 2009 may have been triggered by ascending fluids and/or
286 melts reaching the bottom of the rigid, uppermost layer of the solid basaltic rocks. The presence
287 of some seismicity in this low-attenuation layer above the transition boundary indicates that the
288 pressure in the conduit zone produced cracks in the upper layer but was insufficient to fracture
289 the layer to the surface. It can be seen that the seismicity stopped at an approximate depth of 2
290 km. It may be speculated that the rigid cover prevented a new eruption in the Harrat Lunayyir.
291 However, the facts all indicate the magma sources are still active and that these sources may find
292 a weaker part of the crust in the future to create a conduit to the surface.

293

294 **4. Conclusions**

295 We constructed a 3D model of the seismic attenuation distribution in the crust beneath
296 the Harrat Lunayyir. Although less attenuation data were used compared to the travel time data
297 used by *Hansen et al. (2013)*, we achieved a sufficient resolution thanks to the absence of typical
298 trade-offs between the source and model parameters existing for passive source travel time
299 tomography.

300 The derived model clearly links to the observed geological features and allows the
301 interpretation for the recent seismicity crisis in the Harrat Lunayyir. In the shallow layers, we
302 identified the contrast between the low-attenuation layer within the basalt field and the high-
303 attenuation zones in the surrounding the sedimentary basins. Below 6 km, we found a prominent
304 high-attenuation zone that perfectly confines the narrow seismicity cluster observed in 2009. We
305 propose that this high-attenuation pattern represents the upper portion of a conduit bringing
306 fluids and/or melts from deep sources. Based on the derived attenuation model and seismicity

307 distribution analyses, we conclude that this conduit most likely reached the depth of 6 km
308 corresponding to the bottom of a rigid layer which is composed of basalts erupted during
309 previous eruptions. The elevated pressure caused by the conduit process might create cracks
310 within the rigid layer; however, it was insufficient to fracture fully to the surface. In this sense,
311 this basaltic lid saved the area from a new eruption that may occur if the conduit discovers a
312 weaker part of the crust to ascend.

313 The accumulated seismic records contain significant information on the seismic
314 properties of this activated area, and they are still not fully analyzed. Deriving the S-velocity
315 model and assessing the Vp/Vs distribution will be particularly important and is the next step of
316 our study.

317

318 **Acknowledgements:**

319 The authors extend their appreciation to the Deanship of Scientific Research at King Saud
320 University (Saudi Arabia) for funding the work through the research group project No RGPVPP-
321 122. Special thanks to the Saudi Geological Survey (SGS) for providing waveform data for this
322 study. The work of the Russian participants is supported by Grant RFBR 13-0512056 ofi_m. We
323 are grateful to the anonymous reviewer for constructive criticism and wise recommendations.

324

325 **References**

326 Aki, K.: Scattering and attenuation of shear waves in the lithosphere. *Journal of Geophysical*
327 *Research: Solid Earth (1978–2012)*, 85(B11), 6496-6504, 1980.

328 Aki, K., and Chouet, B.: Origin of coda waves: source, attenuation, and scattering
329 effects. *Journal of Geophysical Research*, 80(23), 3322-3342, 1975.

330 Al-Amri, A.M.S.: Recent seismic activity in the northern Red Sea, *J. Geodyn.*, 20, 243-253,
331 1995.

332 Al-Damegh, K., Sandvol, E., Al-Lazki, A., and Barazangi, M.: Regional seismic wave
333 propagation (Lg and Sn) and Pn attenuation in the Arabian plate and surrounding regions,
334 *Geophys. J. Int.*, 157, 775-795, 2004.

335 Al-Dayel, M.,: Geothermal resources in Saudi Arabia. *Geothermics*, 17(2), 465-476, 1988.

336 Baer, G., and Hamiel Y.: Form and growth of an embryonic continental rift: InSAR observations
337 and modeling of the 2009 western Arabia rifting episode, *Geophys.J. Int.*, 182, 155-167,
338 2010.

339 Camp, V. E., Hooper, P. R., Roobol, M. J., and White, D. L.: The Madinah eruption, Saudi
340 Arabia: Magma mixing and simultaneous extrusion of three basaltic chemical
341 types. *Bulletin of volcanology*, 49(2), 489-508, 1987.

342 Chang, S.J., Merino, M., Van der Lee, S., Stein, S., and Stein, C. A.: Mantle flow beneath Arabia
343 offset from the opening Red Sea, *Geophys. Res. Lett.*, 38, L04301, 2011.

344 Cochran, J. and Martinez, F.: Structure and tectonics of the northern Red Sea: catching a
345 continental margin between rifting and drifting, *Tectonophys.*, 150, 1-32, 1988.

346 Cochran, J.R., and Karner, G.D.: Constraints on the deformation and rupturing of continental
347 lithosphere of the Red Sea, in *Imaging, Mapping, and Modeling Continental Lithosphere*
348 *Extension and Breakup*, edited by G.D. Karner et al., *Geol. Soc. Publ.*, 282, 265-289, 2007.

349 El-Isa, Z.H., and Al-Shanti, A.: Seismicity and tectonics of the Red Sea and western Arabia,
350 *Geophys. J.*, 97, 449-457, 1989.

351 Evans, J. R., and Zucca, J. J.: Active high - resolution seismic tomography of compressional
352 wave velocity and attenuation structure at Medicine Lake Volcano, Northern California
353 Cascade Range. *J.Geoph.Res.* (1978–2012), 93(B12), 15016-15036, 1988.

354 Gusev, A.A. and Abubakirov, I.R.: Vertical profile of effective turbidity reconstructed from
355 broadening of incoherent body wave pulses—I. General approach and the inversion
356 procedure, *Geophys. J. Int.*, 136, 295–308, 1999.

357 Hansen, S., Thurber, C., Mandernach, M., Haslinger, F., and Doran, C.: Seismic velocity and
358 attenuation structure of the east rift zone and south flank of Kilauea Volcano,
359 Hawaii. *Bulletin of the Seismological Society of America*, 94(4), 1430-1440, 2004.

360 Hansen, S. E., DeShon, H. R., Moore-Driskell, M. M., and Al-Amri, A.: Investigating the P
361 wave velocity structure beneath Harrat Lunayyir, northwestern Saudi Arabia, using double-
362 difference tomography and earthquakes from the 2009 seismic swarm. *Journal of*
363 *Geophysical Research: Solid Earth*, 118(9), 4814-4826, 2013.

364 Koulakov I.: LOTOS code for local earthquake tomographic inversion. Benchmarks for testing
365 tomographic algorithms, BSSA, Vol. 99, No. 1, pp. 194-214, 2009.

366 Koulakov, I.: Studying deep sources of volcanism using multiscale seismic tomography, *Journal*
367 *of Volcanology and Geothermal Research*, 257, 205-226, 2013.

368 Koulakov, I., Sobolev S.V., and Asch G.: P- and S-velocity images of the lithosphere-
369 asthenosphere system in the Central Andes from local-source tomographic inversion,
370 *Geophys. Journ. Int.*, 167, 106-126, 2006.

371 Koulakov, I., Bindi, D., Parolai, S., Grosser, H., and Milkereit, C.: Distribution of Seismic
372 Velocities and Attenuation in the Crust Beneath the North Anatolian Fault (Turkey) from
373 Local Earthquake Tomography, *Bull. Seism. Soc. Am.*, 100, issue 1. p. 207-224, 2010.

374 Koulakov, I., El Khrepy, S., Al-Arifi, N., Kuznetsov, P., and Kasatkina, E.: Images of the active
375 magma sources beneath the Lunayyir basaltic field (Saudi Arabia) from local earthquake
376 seismic tomography, *Earth Plan. Sci. Lett.* (in consideration), 2014.

377 Lees, J. M., and Lindley, G. T.: Three - dimensional attenuation tomography at Loma Prieta:
378 Inversion of t^* for Q. *J.Geoph.Res.*, 99(B4), 6843-6863, 1994.

379 Lees, J. M. Seismic tomography of magmatic systems. *Journal of Volcanology and Geothermal*
380 *Research*, 167(1), 37-56, 2007.

- 381 Martínez-Arévalo, C., Patanè, D., Rietbrock, A., and Ibáñez, J. M.: The intrusive process leading
382 to the Mt. Etna 2001 flank eruption: Constraints from 3-D attenuation
383 tomography. *Geophysical Research Letters*, 32(21), L21309, 2005.
- 384 Paige, C.C., and Saunders, M.A.: LSQR: An algorithm for sparse linear equations and sparse
385 least squares, *ACM Trans. Math. Soft*, 8, 43-71, 1982.
- 386 Pallister, J.S., McCausl, W.A., Jónsson, S., Lu Z.H.M., El Hadidy, S., Aburukbah, A., Stewart,
387 I.C.F., Lundgren, P.R., White, R.A., and Moufti, M.R.H.: Broad accommodation of rift-
388 related extension recorded by dyke intrusion in Saudi Arabia. *Nature Geosciences* 3: 705–
389 712, 2010.
- 390 Rautian, T. G., and Khalturin, V. I.: The use of the coda for determination of the earthquake
391 source spectrum. *Bulletin of the Seismological Society of America*, 68(4), 923-948, 1978.
- 392 Sato, H., and Fehler M. C.: *Seismic Wave Propagation and Scattering in the Heterogeneous*
393 *Earth*, AIP, New York, 308 pp., 1998.
- 394 Schurr, B., Asch, G., Rietbrock, A., Trumbull, R., and Haberland, C. H.: Complex patterns of
395 fluid and melt transport in the central Andean subduction zone revealed by attenuation
396 tomography. *Earth and Planetary Science Letters*, 215(1), 105-119, 2003.
- 397 Zobin, V. M., Al-Amri, A. M., and Fnais, M.: Seismicity associated with active, new-born, and
398 re-awakening basaltic volcanoes: case review and the possible scenarios for the Harraat
399 volcanic provinces, Saudi Arabia. *Arabian Journal of Geosciences*, 6(2), 529-541, 2013.

400

401 **Figure captions:**

402 Figure 1. Study region in the framework of regional tectonics and data distribution. A.

403 Topographic map of the Arabian Peninsula. The dotted line indicates the boundary between
404 the Arabian Shield and the Arabian Platform. The reddish spots mark the Cenozoic basaltic
405 fields (harrats) with their activity ages. The black rectangle is the location of the Harraat

406 Lunayyir. B. Zoom in of the study area. The triangles show the seismic stations, and the
407 yellow dots mark the event locations used in this study.

408 Figure 2. Velocity model (P-, S-anomalies and Vp/Vs ratio) and local source hypocenters (black
409 dots) from Koulakov et al. (2014) in two vertical sections with the same locations as shown
410 in Figure 7. This model and source coordinates were used to construct the rays for the
411 attenuation tomography in this study.

412 Figure 3. Schematic representation of the basic principle used for the attenuation inversion in this
413 study. Hatches are the scatters which are roughly uniformly distributed within the study
414 area. Red and blue indicate zones of high and low attenuation, respectively. Star is a source;
415 triangles are the receivers; black lines are the direct and scattered rays between source and
416 receivers. Above: schematic seismograms recorded at stations A and B corresponding to
417 low and high attenuation areas. Dotted lines are the envelopes of the seismograms. Lines
418 indicated with S and S+1s mark the arrival time of the S-wave and 1 second later point.

419 Figure 4. Workflow for the data analysis. A. Initial seismogram is narrow-band filtered at 3 Hz.
420 The red lines indicate the analyzed time interval. B. An envelope of absolute deviations in
421 the seismogram. C. Logarithmic transformation of the envelope. The red line indicates the
422 linear approximation with the best fit. The slope of this line was then converted into the
423 quality factor.

424 Figure 5. Attenuation distributions and source locations in vertical sections based on the 1D
425 velocity model. This model can be compared with the main model in Figure 6 derived in
426 the 3D model. Locations of the profiles are shown in Figure 6.

427 Figure 6. Resulting 3D distribution of the attenuation in four horizontal and two vertical sections.
428 The dots indicate seismic events near the sections. The triangles are the seismic stations.
429 The black line is the boundary of the basaltic field.

430 Figure 7. Results of synthetic modeling for the attenuation tomography. Black lines indicate the
431 limits of the synthetic anomalies. At 6 km depth, the anomalies change the sign. Triangles

432 indicate the seismic stations. The contour of the basalt fields is given by brown line for the
433 reference.

434 Figure 8. Comparison of the inversion results obtained for the data corresponding to three
435 frequencies: 1.5, 3 and 6 Hz. The results are presented for 2 km and 10 km depth. The
436 triangles are the seismic stations. The black line is the boundary of the basaltic field.

437

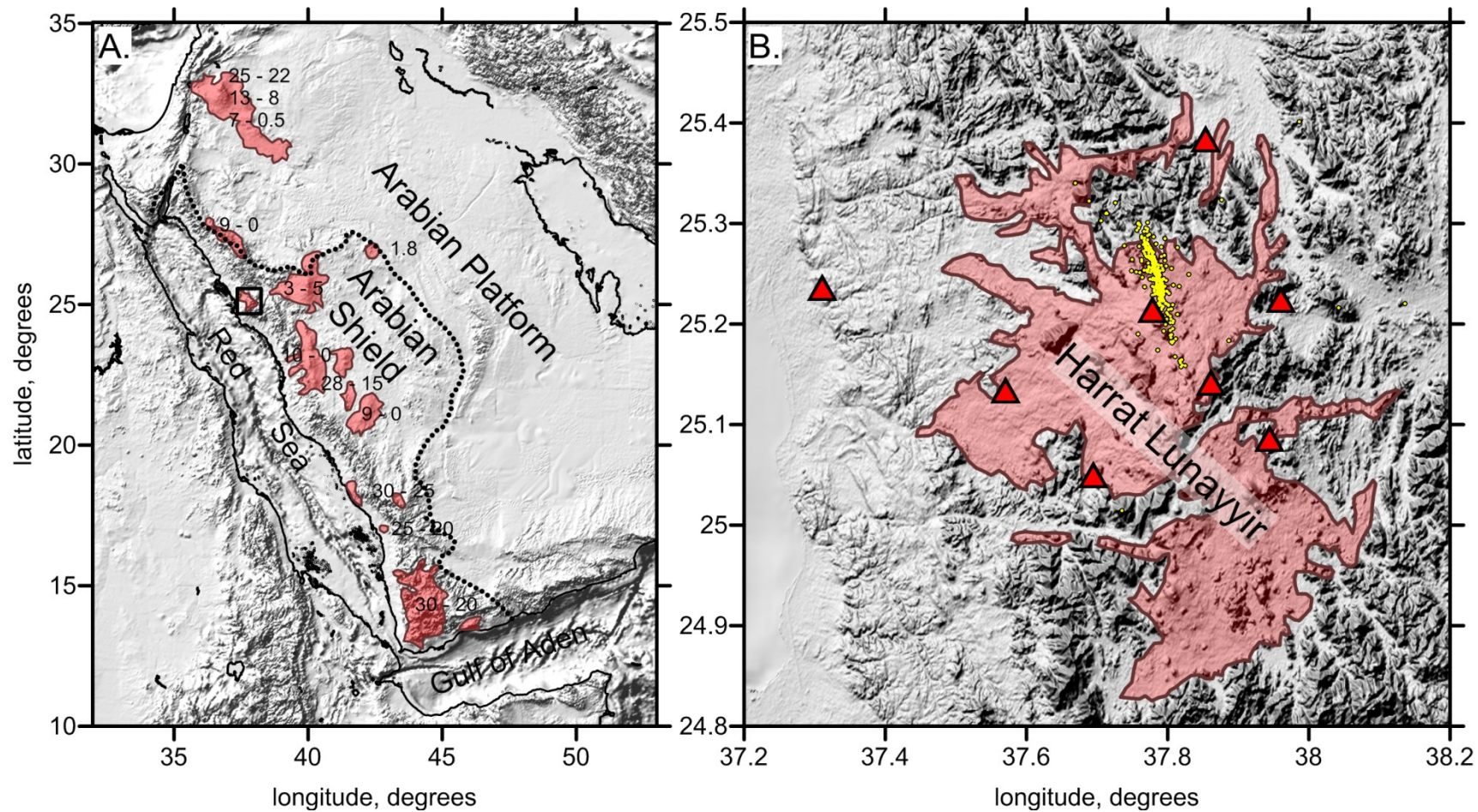


Figure 1. Study region in the framework of regional tectonics and data distribution. A. Topographic map of the Arabian Peninsula. The dotted line indicates the boundary between the Arabian Shield and the Arabian Platform. The reddish spots mark the Cenozoic basaltic fields (harrats) with their activity ages. The black rectangle is the location of the Harrat Lunayyir. B. Zoom in of the study area. The triangles show the seismic stations, and the yellow dots mark the event locations used in this study.

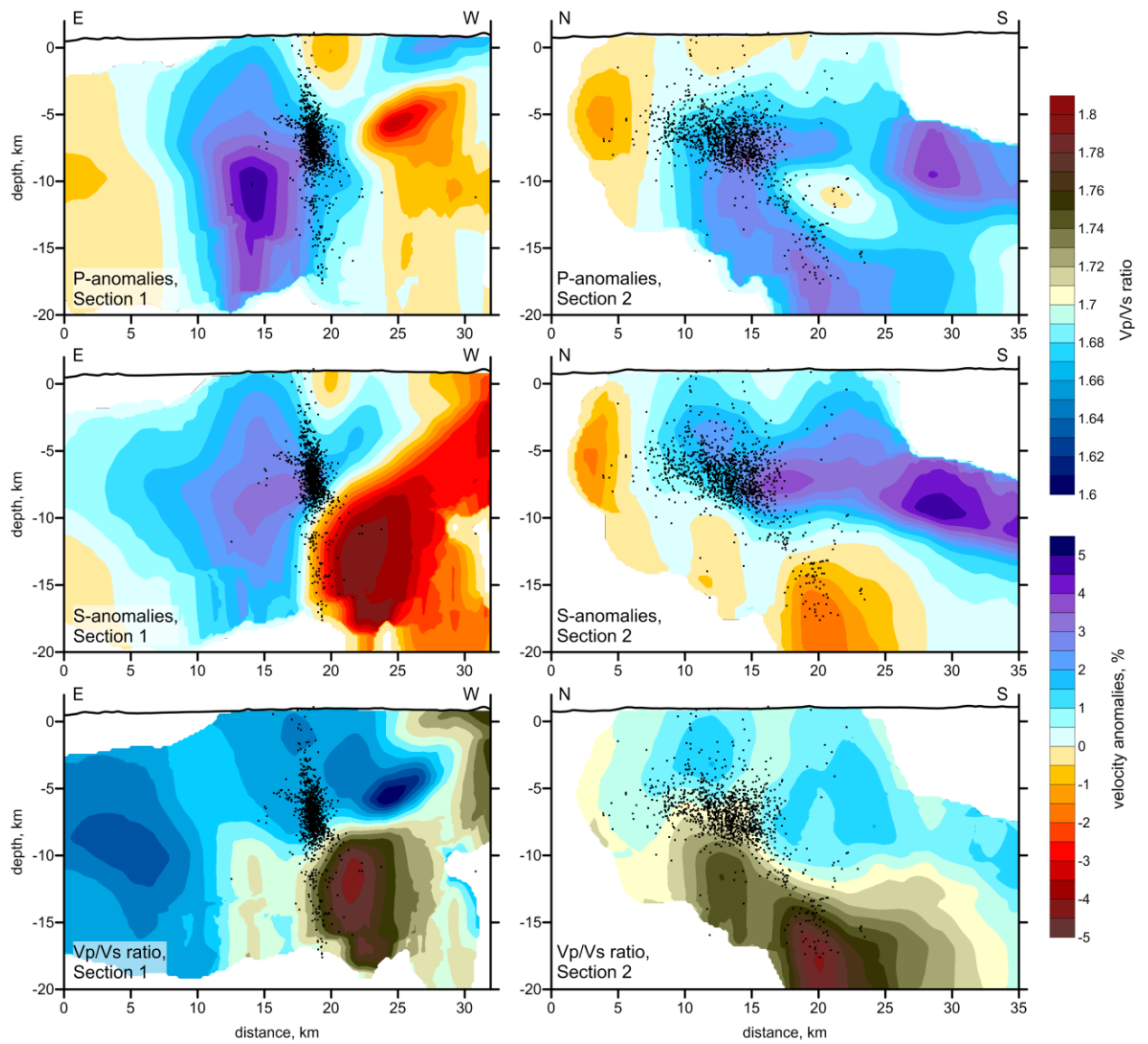


Figure 2. Velocity model (P-, S-anomalies and Vp/Vs ratio) and local source hypocenters (black dots) from Koulakov et al. (2014) in two vertical sections with the same locations as shown in Figure 7. This model and source coordinates were used to construct the rays for the attenuation tomography in this study.

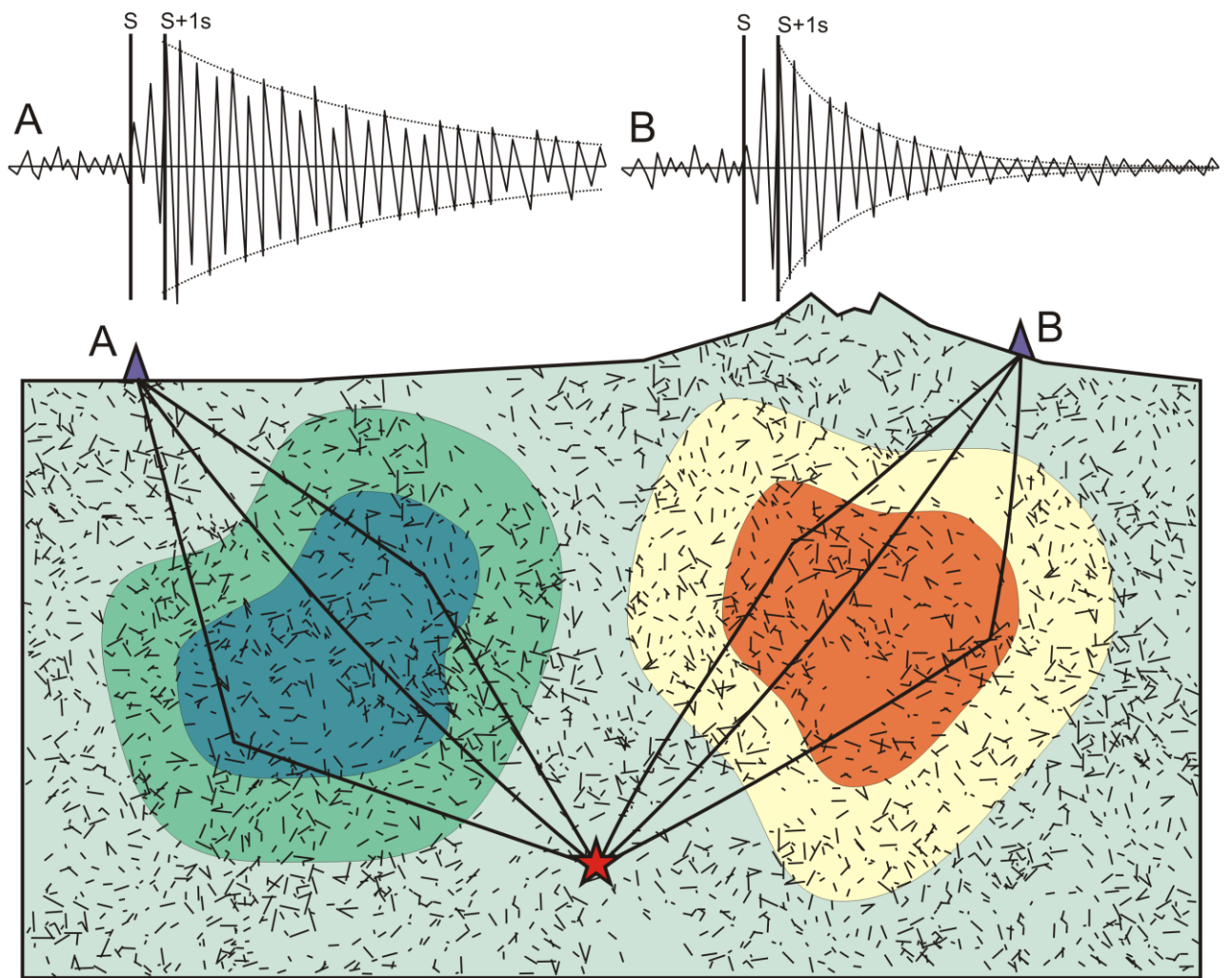


Figure 3. Schematic representation of the basic principle used for the attenuation inversion in this study. Hatches are the scatters which are roughly uniformly distributed within the study area. Red and blue indicate zones of high and low attenuation, respectively. Star is a source; triangles are the receivers; black lines are the direct and scattered rays between source and receivers. Above: schematic seismograms recorded at stations A and B corresponding to low and high attenuation areas. Dotted lines are the envelopes of the seismograms. Lines indicated with S and S+1s mark the arrival time of the S-wave and 1 second later point.

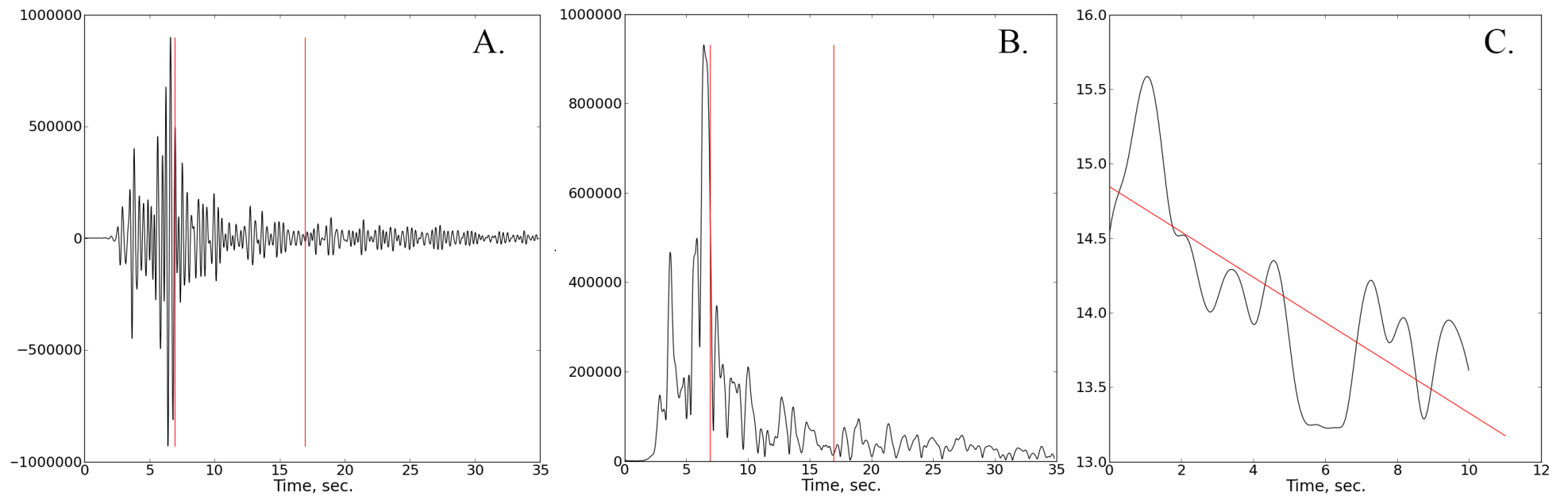


Figure 4. Workflow for the data analysis. A. Initial seismogram is narrow-band filtered at 3 Hz. The red lines indicate the analyzed time interval. B. An envelope of absolute deviations in the seismogram. C. Logarithmic transformation of the envelope. The red line indicates the linear approximation with the best fit. The slope of this line was then converted into the quality factor.

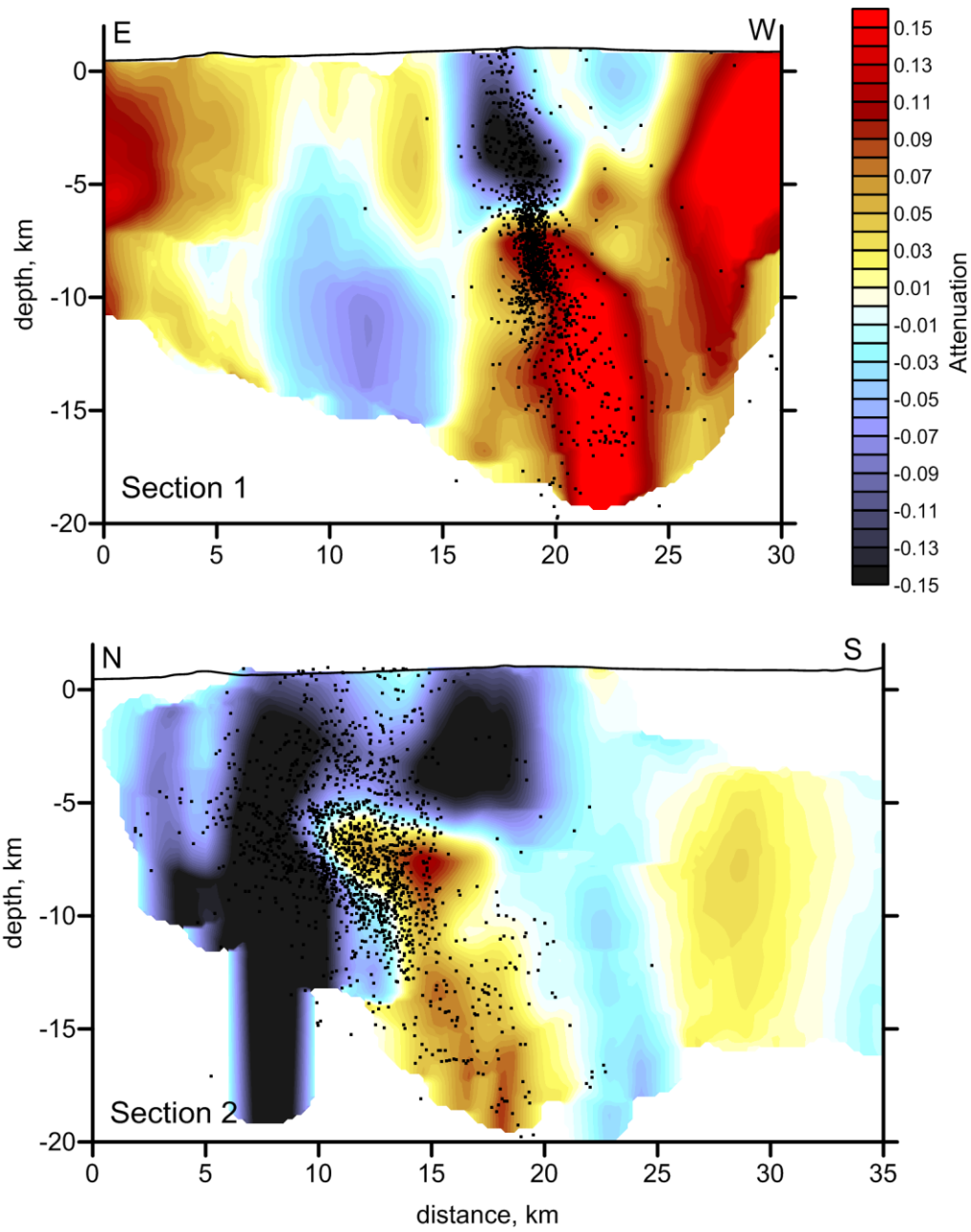


Figure 5. Attenuation distributions and source locations in vertical sections based on the 1D velocity model. This model can be compared with the main model in Figure 6 derived in the 3D model. Locations of the profiles are shown in Figure 6.

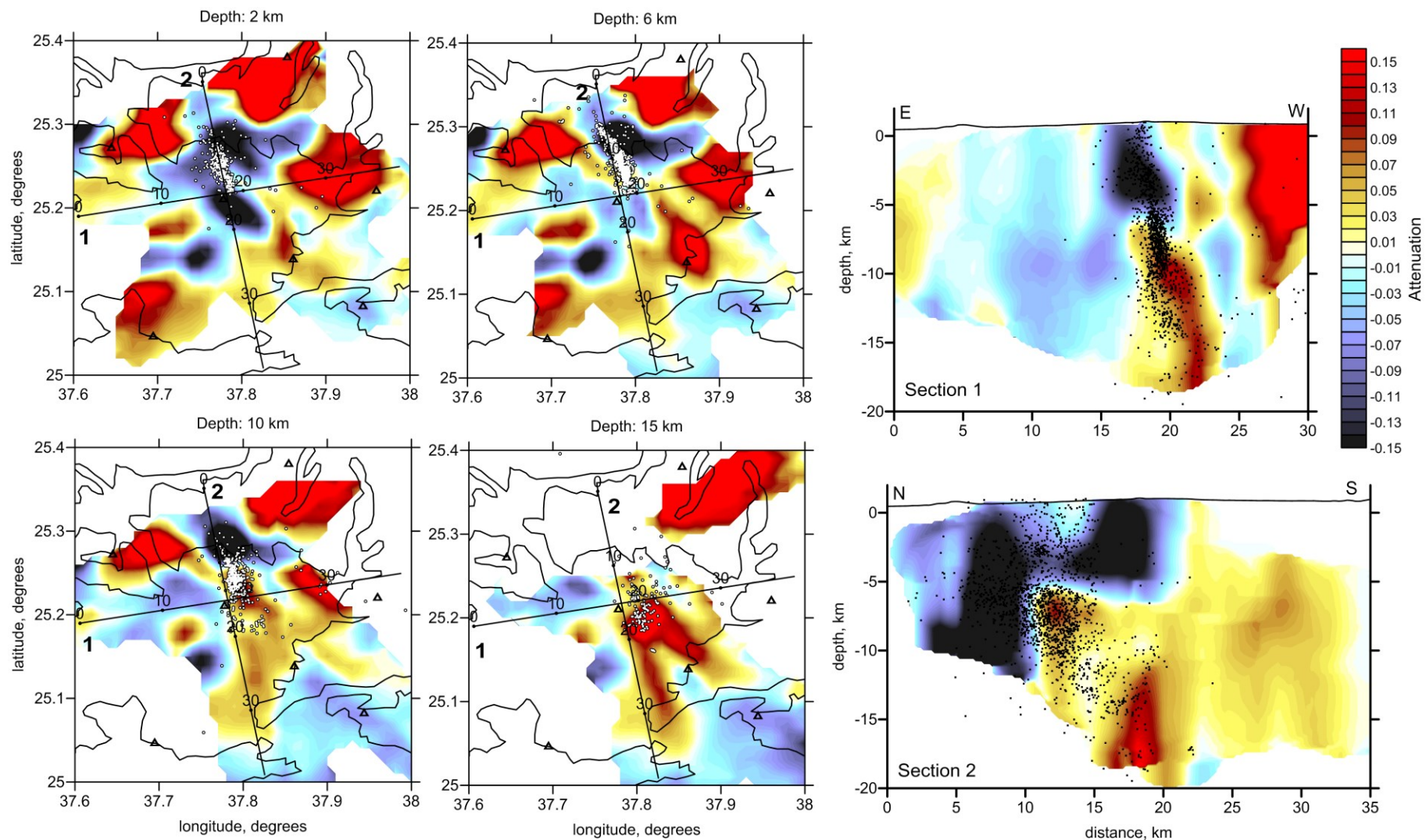


Figure 6. Resulting 3D distribution of the attenuation in four horizontal and two vertical sections. The dots indicate seismic events near the sections. The triangles are the seismic stations. The black line is the boundary of the basaltic field.

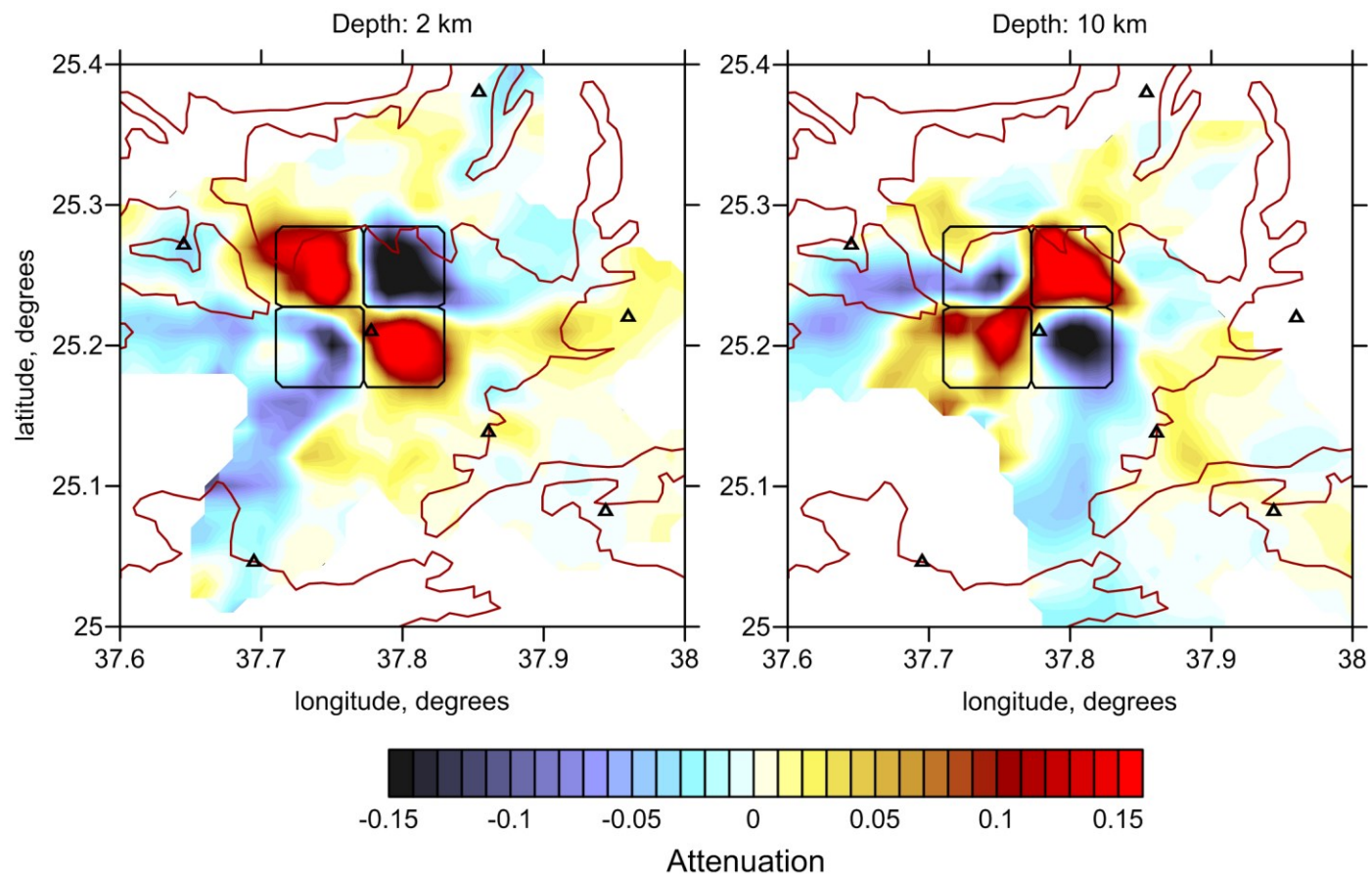


Figure 7. Results of synthetic modeling for the attenuation tomography. Black lines indicate the limits of the synthetic anomalies. At 6 km depth, the anomalies change the sign. Triangles indicate the seismic stations. The contour of the basalt fields is given by brown line for the reference.

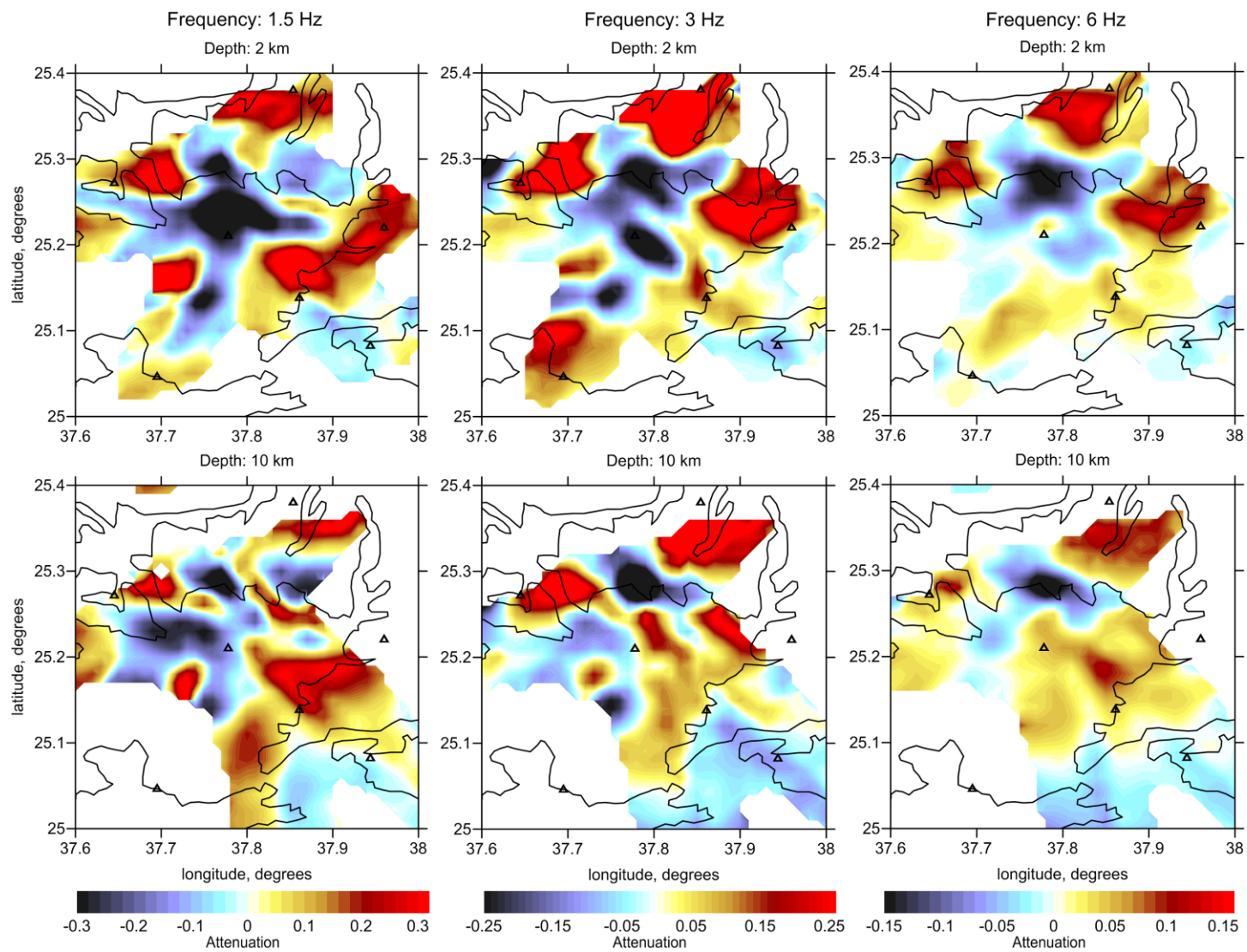


Figure 8. Comparison of the inversion results obtained for the data corresponding to three frequencies: 1.5, 3 and 6 Hz. The results are presented for 2 km and 10 km depth. The triangles are the seismic stations. The black line is the boundary of the basaltic field.